



Molybdenum-modified and vertex-reinforced quaternary hexapod nano-skeletons as efficient electrocatalysts for methanol oxidation and oxygen reduction reaction



Lei Huang^a, Min Wei^a, Ning Hu^a, Panagiotis Tsiakaras^{b,c,d,*}, Pei Kang Shen^{a,*}

^a Collaborative Innovation Center of Sustainable Energy Materials, Guangxi Key Laboratory of Electrochemical Energy Materials, State Key Laboratory of Processing for Non-ferrous Metal and Featured Materials, Guangxi University, Nanning, 530004, PR China

^b Laboratory of Materials and Devices for Clean Energy, Ural Federal University, 19 Mira Str., Yekaterinburg, 620002, Russia

^c Laboratory of Electrochemical Devices based on Solid Oxide Proton Electrolytes, Institute of High Temperature Electrochemistry (RAS), Yekaterinburg, 620990, Russia

^d Laboratory of Alternative Energy Conversion Systems, Department of Mechanical Engineering, School of Engineering, University of Thessaly, Pedion Areos, 38834, Greece

ARTICLE INFO

Keywords:

Quaternary hexapod nano-skeletons
High-index facets
Vertex-reinforced
Methanol oxidation reaction
Oxygen reduction reaction

ABSTRACT

Noble metal binary and ternary catalysts have become a new class of fuel cell electrocatalysts due to their high catalytic activity. However, improvement is still necessary to reduce the consumption of Pt and obtain the quaternary Pt-based catalyst by Mo modification. Through the introduction of $\text{Mo}(\text{CO})_6$, novel quaternary hexapod nano-skeletons with high-index facets are obtained here, which are composed of core, first-layer feet and second-layer feet. Compared with PtCoNi nano-particles (NPs), the vertex-reinforced PtCoNiMo hexapod nano-skeletons (NSs), due to abundant tip areas, can facilitate electron transfer and mass exchange. It is found that the as prepared PtCoNiMo nano-skeletons catalyst exhibits enhanced mass activity, stability and anti-poisoning ability towards methanol oxidation reaction and oxygen reduction reaction, compared to commercial Pt/C catalyst and PtCoNi nanoparticles. More importantly, the development of quaternary catalysts can create better possibilities for the performance improvement of Pt-based catalysts.

1. Introduction

Though non-noble metal catalysts have received considerable attention and development, Pt-based catalysts are still necessary nanomaterials in the catalytic reactions due to their superior catalytic properties [1,2]. For current commercial Pt-based catalysts, the main challenge comes from limited Pt resources and high application costs. At the same time, it also faces the issue of poor catalytic activity, stability and anti-poisoning ability. To address these challenges, we consider the synthesis of binary, ternary or even multi-element low Pt-based catalysts by introducing other metallic elements [3–5].

Among various catalyst composition, binary and ternary Pt-based catalysts (e.g. Pt-Cu [6], Pt-Ni [7], Pt-Co [8], Pt-Pd [9], Pt-Ru [10], Pt-Au [11], Pt-Cu-Ni [12], Pt-Cu-Co [13], Pt-Co-Ni [14], etc.) have been broadly investigated in recent years and have shown enhanced catalytic performance, stability and anti-poisoning ability than commercial Pt/C catalyst. However, improvement is still continuous, and superior catalysts also need to be further studied. More and more researchers are beginning to understand the quaternary Pt-based catalysts and explore

their applications in electrocatalysis [15,16]. To reduce the consumption of Pt and the cost of the catalyst, we have long been committed to developing Mo-modified multi-element Pt-based catalysts, and improve catalytic performance, stability and anti-poisoning ability of Pt-based catalysts.

The high-efficiency catalysts are mainly hollow spheres, nanoframes and nano-skeletons. For this type of catalytic material, they exhibit a highly open structure and efficient atomic utilization. Electron transfer and mass exchange are accelerated in electrochemical tests, which is very beneficial for improving catalytic performance. It is well known that carbonyl compounds ($\text{M}_x(\text{CO})_y$, $\text{M} = \text{Fe, Co, W, Mo, etc.}$) as surfactants and reducing agents play an important role in the preparation of many nanomaterials, such as the synthesis of nanowire [17], concave cube [18], nanorod [19], etc. Carbonyl compounds are popular in the synthesis of nanomaterials due to the presence of carbonyl groups in its organic composition [20–23]. In addition, carbonyl compounds are safe and convenient compared to CO gas, which is good for controlling the synthesis and growth of nanocrystals. Due to these advantages, carbonyl compounds are a great choice for our material synthesis [24].

* Corresponding authors.

E-mail addresses: tsiak@mie.uth.gr (P. Tsiakaras), pkshen@gxu.edu.cn (P. Kang Shen).



Fig. 1. Schematic diagram of preparation and formation of PtCoNiMo hexapod nano-skeletons (NSs).

Herein, we report vertex-reinforced quaternary PtCoNiMo hexapod nano-skeletons (NSs), achieved by introduction of $\text{Mo}(\text{CO})_6$, for efficient oxygen reduction catalysis and methanol oxidation catalysis. Obviously, $\text{Mo}(\text{CO})_6$ also plays a significant part throughout the synthesis, and only PtCoNi NPs can be obtained in absence of $\text{Mo}(\text{CO})_6$. The quaternary PtCoNiMo NSs possess abundant tip areas with high-index facets, which can promote efficiency of electronic transfer and mass exchange. Therefore, the quaternary PtCoNiMo hexapod NSs exhibit efficient mass activity, stability and anti-poisoning ability for methanol oxidation reaction (MOR) and oxygen reduction reaction (ORR), compared to commercial Pt/C catalyst and to PtCoNi NPs.

2. Experimental section

2.1. Reagents

Platinum (II) acetylacetone [$\text{Pt}(\text{acac})_2$, 98%], cobalt (III) acetylacetone [$\text{Co}(\text{acac})_3$, 98%], nickel (II) acetylacetone [$\text{Ni}(\text{acac})_2$, 98%], molybdenum hexacarbonyl [$\text{Mo}(\text{CO})_6$, 98%], glucose ($\text{C}_6\text{H}_{12}\text{O}_6\cdot\text{H}_2\text{O}$, 99%) and oleylamine (OAM, 80–90%) were bought from Aladdin. The reagents were used as received without further treatment. The solvents (ethanol, n-hexane and n-butylamine) were used in the experiment without any treatment.

2.2. Synthesis of PtCoNiMo hexapod nano-skeletons (NSs)

In a typical synthesis, 10.0 mg of $\text{Pt}(\text{acac})_2$, 9.0 mg of $\text{Co}(\text{acac})_3$ and 6.5 mg of $\text{Ni}(\text{acac})_2$ were dissolved in a glass bottle containing 5 ml of OAM, followed by the addition of 60 mg of glucose and 5 mg of $\text{Mo}(\text{CO})_6$. After stirring for 10 min, it was sonicated until the solution was evenly mixed. It was then transferred to an oil bath at 120 °C for 5 h, and the as obtained product was collected by centrifugation.

2.3. Materials characterization

X-ray powder diffraction (XRD) patterns were performed at 40 kV and 30 mA using a SmartLab3 X-ray diffractometer (Rigaku, Japan) with $\text{Cu K}\alpha$ radiation ($\lambda = 1.5405 \text{ \AA}$). Transmission electron microscopy (TEM), High-resolution TEM (HRTEM) and high-angle annular dark field scanning TEM (HAADF-STEM) images were obtained at 300 kV using a TITAN G2 microscope (FEI, American) equipped with an energy dispersive X-ray spectroscopy (EDS) detector. Moreover, the EDS

mapping images were collected using a 60–300 electron microscope (300 kV). X-ray photoelectron spectroscopy (XPS) measurements were recorded to analyze the chemical composition of the products in an ESCALAB 250 Xi (Thermo Fisher Scientific, USA) with a monochromatic Al X-ray source. In addition, the test data of binding energy were corrected, on the basis of C1s (284.8 eV). The Pt loadings in the catalysts were precisely measured through inductively coupled plasma optical emission spectroscopy (ICP-OES - model PerkinElmer Optima 8000DV), and the mass activity was further obtained according to Pt loadings.

2.4. Electrochemical measurements

The electrochemical measurements were performed in a three-electrode test system by using a rotating ring-disk electrode (RRDE) with a bipotentiostat (Pine, USA). The three-electrode electrochemical system was mainly composed of: i) a glassy carbon electrode (0.196 cm^2) supporting a thin catalyst film (working electrode), ii) a saturated calomel electrode (SCE), or a reversible hydrogen electrode (RHE), (reference electrode), and iii) a graphite rod (counter electrode). In N_2 -saturated 0.5 M H_2SO_4 solution, the cyclic voltammogram (CV) curves were recorded at a sweep rate of 50 mV s^{-1} . The electrochemical surface areas (ECAs) were obtained by integrating the coulombic charges for hydrogen adsorption. As for CO-stripping measurements, the working electrode was held at -0.14 V vs. SCE, and the CV curves were then recorded in a 0.5 M H_2SO_4 solution with a sweep rate of 50 mV s^{-1} . The MOR curves were recorded ($-0.2 \sim 1.0 \text{ V}$ vs. SCE) under a scan rate of 50 mV s^{-1} in a solution of 0.5 M H_2SO_4 and 1.0 M CH_3OH . The ORR polarization curves were recorded ($0.05 \sim 1.1 \text{ V}$ vs. RHE) under a scan rate of 10 mV s^{-1} and 0.1 M HClO_4 solution. In addition, the accelerated durability tests (ADTs) were used to evaluate the stability of the catalysts, which were carried out through performing cyclic potential sweeps.

3. Results and discussions

3.1. Structural analysis of materials

In Fig. 1, a schematic diagram of the preparation and formation of PtCoNiMo hexapod nano-skeletons (NSs) can be seen. In a typical synthesis, $\text{Pt}(\text{acac})_2$, $\text{Ni}(\text{acac})_2$ and $\text{Co}(\text{acac})_3$ are used as reaction

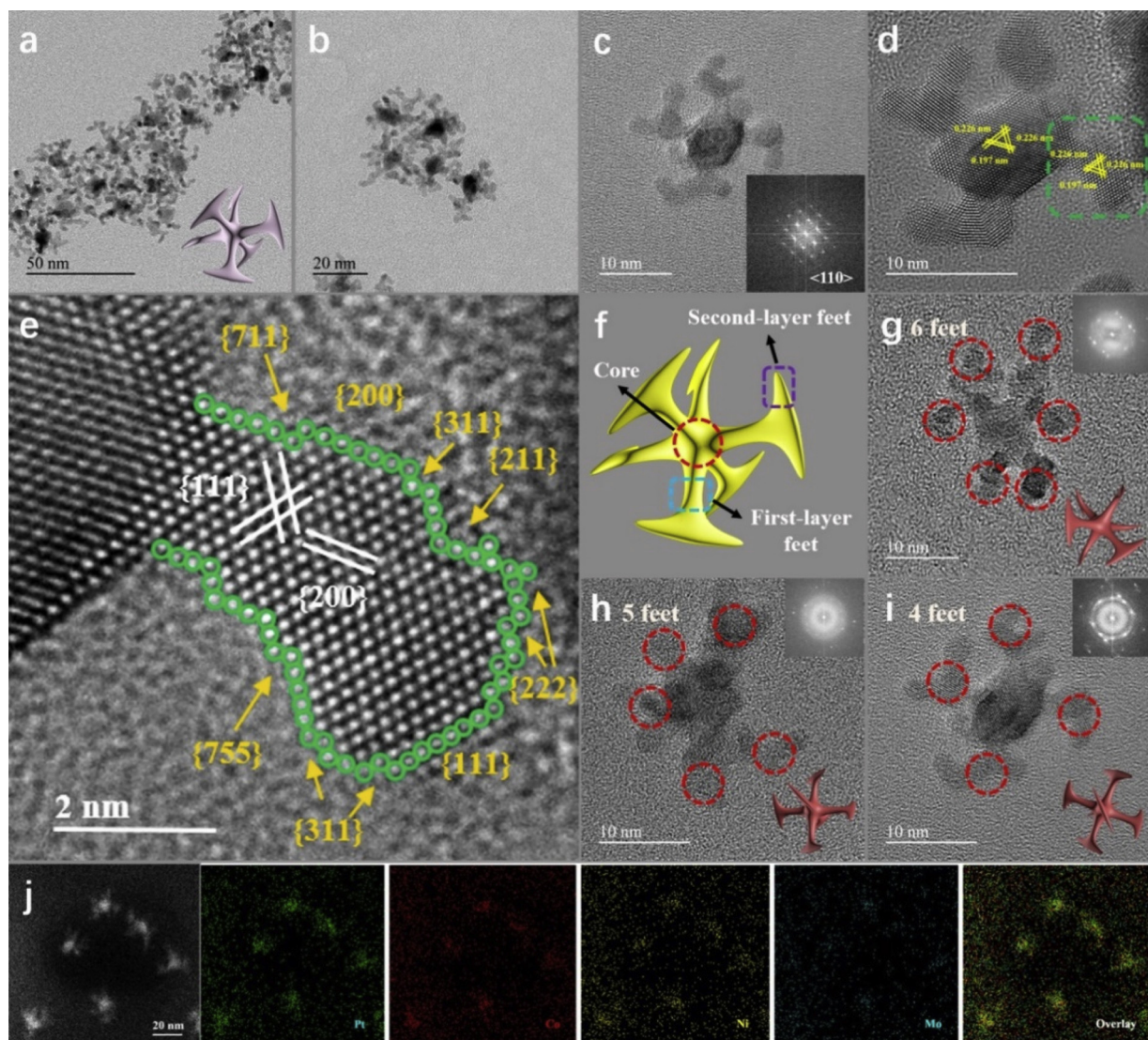


Fig. 2. (a, b) Low-magnification TEM image, (c, d) high-magnification TEM image, (e) atomic-scale HRTEM image, (f) the model and structure, (g, h, i) high-magnification TEM images, corresponding models and FFT images at different angles. (j) EDS mapping images of PtCoNiMo hexapod NSs.

precursors, glucose is used as reducing agent, and $\text{Mo}(\text{CO})_6$ is used as surfactant and reducing agent; all of them are dissolved in OAM reaction solvent by magnetic stirring [25]. Immediately after the sonication for 30 min, a homogeneous mixed solution was obtained. The mixture was then transferred to an oil bath at 120 °C for 5 h. At the same time, the formation process of PtCoNiMo hexapod NSs is simply shown, and the nanocrystal structure undergoes some significant changes as the reaction time progresses. A more detailed evolution process of the nanocrystals is presented below.

For a better analysis of PtCoNiMo hexapod NSs, the typical TEM and HAADF-STEM images of PtCoNiMo nanocrystals display relatively uniform NSs (Figure S1). As shown in Figs. 2a-2d, the structure of PtCoNiMo hexapod NSs can be clearly distinguished, while the structural characteristics of a single nanocrystal were further analyzed through HRTEM images. The atomic-scale HRTEM images obtained from the corresponding dotted squares, and the lattice spacing of 0.226 and 0.197 nm at the center and the tip areas can be recorded according to Fast Fourier Transform (FFT) imaging. Meanwhile, combined with the value of the lattice spacing, the basic crystal facets ($\{111\}$ and $\{200\}$) are also confirmed. It is worth noting that abundant stepped atoms and different high-index facets are observed around the tip area (Fig. 2e), such as $\{211\}$, $\{222\}$, $\{311\}$, $\{711\}$, and $\{755\}$, which can

boost electron transfer, mass exchange and performance improvement in the electrocatalytic reactions [26–29]. To clarify the specific morphology of the PtCoNiMo hexapod NSs, the TEM images obtained at different angles are analyzed (Figure S2). As shown in Fig. 2f, the PtCoNiMo nano-skeletons (NSs) are composed of a central core and first and second-layer feet; the same product can get different images from different perspectives.

As can be distinguished from the high-magnification TEM images (2g-2i), the first image shows 4 feet (Fig. 2g), the second image shows 5 feet (Fig. 2h), and the third image shows 6 feet (Fig. 2i). Through the rotation of the model, the corresponding NSs in the HRTEM images can be clearly observed, which also proves that the PtCoNiMo nanocrystals possess 6 feet [30]. In addition, the FFT images, insets in the TEM images, are clear and bright, indicating that PtCoNiMo hexapod NSs have good crystallinity. Moreover, the EDS mapping images show that the Pt, Co, Ni, Mo are evenly distributed on the PtCoNiMo NSs, and the Mo element is less relative to other metal elements (Figs. 2j & S3). The length of NSs is an important information datum, which has a certain reference value for evaluating the catalytic properties of materials. As shown in Figure S4, the PtCoNiMo hexapod NSs consist of three parts, including central core, first-layer and second-layer feet. The average length d_1 of the central core is ~5.83 nm, the average length d_2 of first-

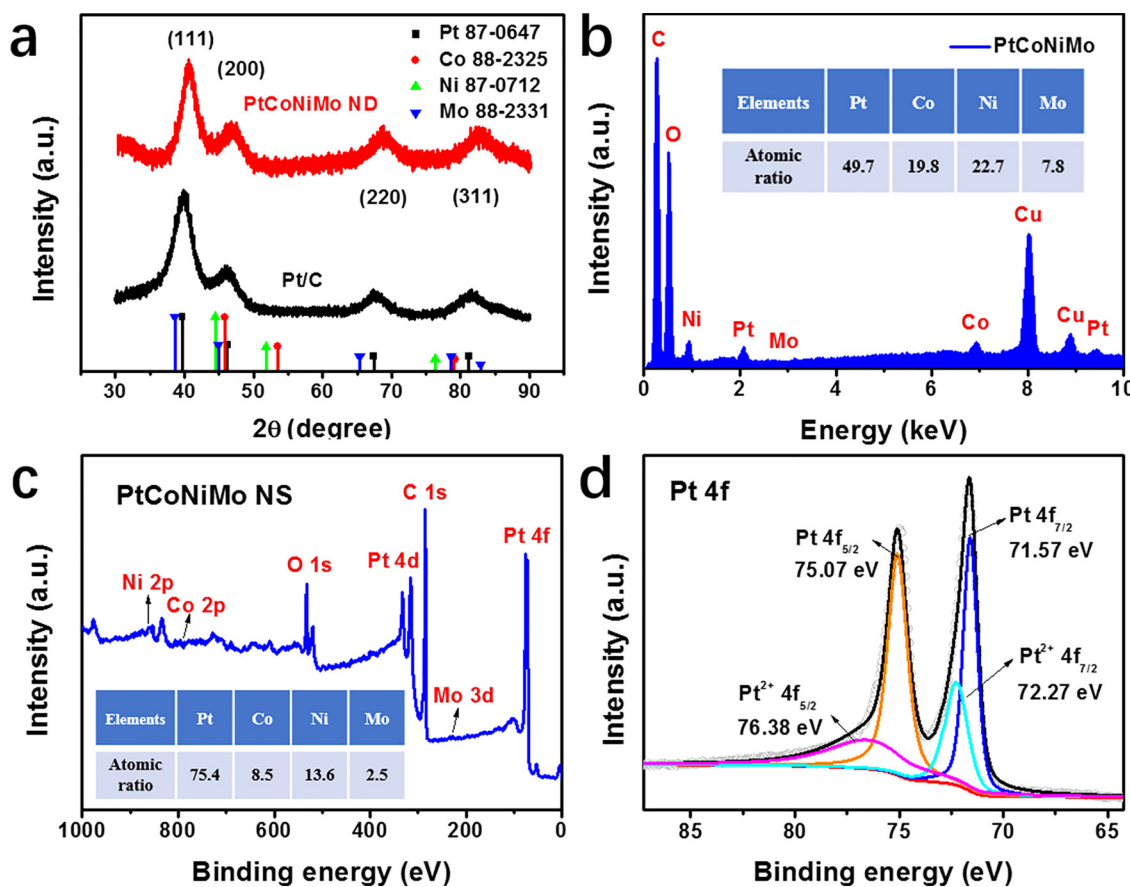


Fig. 3. (a) XRD patterns, (b) TEM-EDS spectrum, (c) XPS survey, (d) Pt 4f spectra of PtCoNiMo hexapod nano-skeletons (NSs).

layer feet is \sim 5.63 nm, and the average length d_3 of the second-layer feet is \sim 4.78 nm. This information shows that the first and second-layer feet occupy a large part of the size of the entire nanocrystal, which is very advantageous for the catalytic performance of the nanomaterial [31–33].

The XRD patterns of the PtCoNiMo hexapod nano-skeletons (NSs) were obtained in order to analyze the crystal structure (Fig. 3a). It is worth notice that the diffraction peaks of PtCoNiMo hexapod NSs are at 40.72° , 47.15° , 68.93° and 82.86° , which are closely related to some specific crystal facets based on the position of 2θ diffraction peak, including (111), (200), (220), and (311). Moreover, the XRD patterns of the PtCoNiMo hexapod NSs have a significantly positive shift compared to commercial Pt/C, and no impurity peaks were observed. The introduction of Co, Ni, Mo decreases the interatomic distances and redesign the electronic structure of Pt atoms. Meanwhile, the TEM-EDS spectrum shows that the atomic ratio of Pt/Co/Ni/Mo equals 49.7/19.8/22.7/7.8, and the results can be used as a reference to analyze the elemental composition (Fig. 3b). To further analyze the PtCoNiMo NSs, the XPS measurements were carried out. As shown in Figs. 3c & 3d, the XPS survey displays the atomic ratio of Pt/Co/Ni/Mo equals 75.4/8.5/13.6/2.5. It is worth noting that the materials have a 75.4% Pt atomic ratio, demonstrating that the PtCoNiMo NSs possess a Pt-rich surface. The Pt 4f area of PtCoNiMo hexapod NSs can be cleaved into Pt $4f_{7/2}$ and Pt $4f_{5/2}$, the first group Pt $4f_{7/2}$ and $Pt^{2+} 4f_{7/2}$ at 71.57 and 72.27 eV, and the other group Pt $4f_{5/2}$ and $Pt^{2+} 4f_{5/2}$ at 75.07 and 76.38 eV, where the metal Pt is zero valence, and the metal oxides on the surface is divalent. Compared with that of pure Pt, the Pt 4f binding energy of PtCoNiMo hexapod NSs has an obviously negative shift, demonstrating that the electronic structure of Pt is redesigned.

Combining the shift of Pt 4f, Ni 2p, Mo 3d and Co 2p spectra (Figures S5), we conclude that the electronic structures of Pt have been

optimized and redesigned due to introduction of Co, Ni and Mo atoms [34–36].

3.2. Growth process analysis

To carefully clarify the formation process of quaternary PtCoNiMo hexapod NSs, the morphological evolution of the nanocrystal was considered with the progress of reaction time. As shown in Fig. 4, Pt species are preferentially reduced and form nuclei due to standard redox potential in the entire reaction system, and then other species will gradually be deposited [37,38]. NPs (nanoparticles) were obtained when the reaction was carried out for 1 h. Generally, the surface energy of the (100) facets is greater than that of (111) facets, indicating that the latter is more stable. As the CO molecules adsorb on the top of Pt (111), the (111) facet becomes more stable, resulting in deposition of various species along a specific direction of $<100>$ [39–41]. In the subsequent growth phase, the reaction lasted for 2 h and the NP with the first-layer of feet was collected. As the reaction time progresses, the particle size of the nanocrystals increases, and the second-layer feet was formed due to excessive growth. After 5 h of reaction time, PtCoNiMo hexapod NS was synthesized.

The above discussion and investigation, further demonstrated that $Mo(CO)_6$ is vital throughout the synthesis process and the formation of vertex-reinforced PtCoNiMo NSs structure is reasonable [42–44]. $Mo(CO)_6$ is usually used to adjust the morphology as a structure directing agent, PtCoNiMo NSs can be obtained only in the presence of 5 mg $Mo(CO)_6$ in the reaction system, and the PtCoNi NPs were synthesized in the absence of $Mo(CO)_6$. When 1, 3 mg $Mo(CO)_6$ was added, only a small amount of crystals with feet are obtained (Figure S6). The results further indicate that $Mo(CO)_6$ plays an important role in the reaction system, and the PtCoNiMo hexapod NSs can be obtained when there is

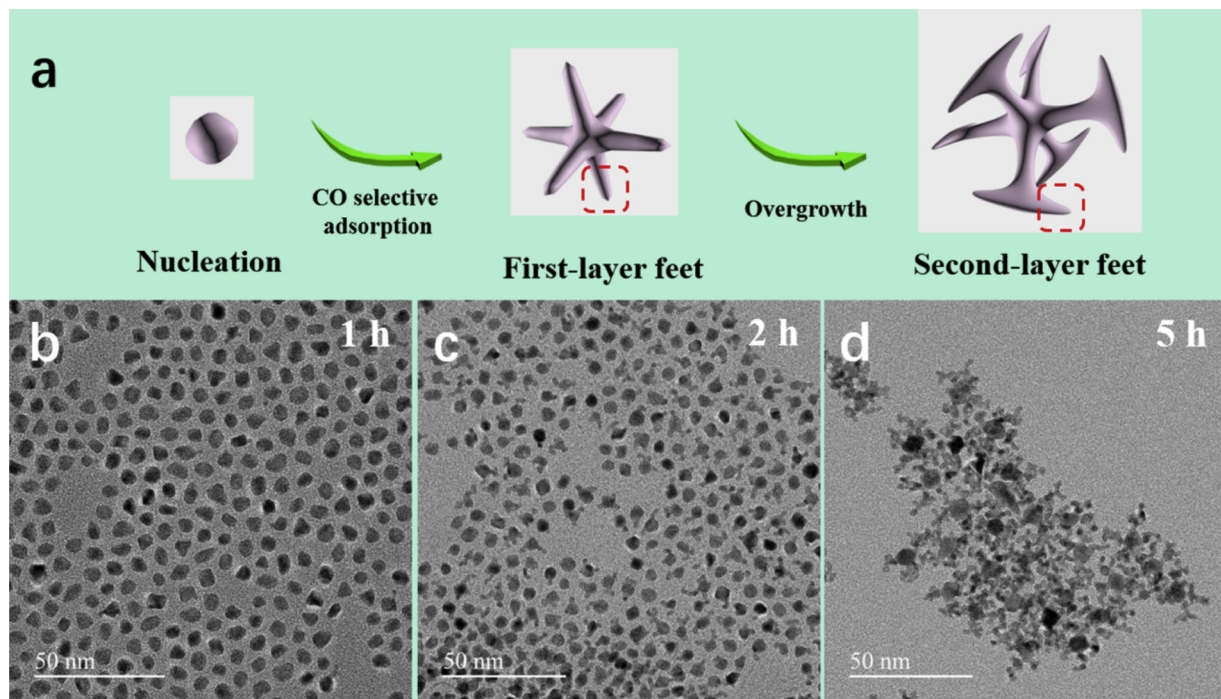


Fig. 4. (a) Schematic of the major steps involved in the formation of the PtCoNiMo hexapod NSs. TEM images of PtCoNiMo hexapod NSs prepared at different reaction time (b) 1 h, (c) 2 h and (d) 5 h, respectively.

enough amount of $\text{Mo}(\text{CO})_6$.

3.3. Electrochemical performance analysis

Before the electrocatalytic measurements, PtCoNiMo hexapod NSs catalyst was loaded onto commercial carbon. As shown in Table S1, the mass activity of the catalysts was obtained based on Pt loadings. Meanwhile, commercial Pt/C catalyst is used as a basic standard for comparing the catalytic performance of other catalysts. In Fig. 5a, a schematic diagram of MOR and ORR processes is depicted, indicating ORR at the cathode and MOR at the anode are important in direct methanol fuel cells (DMFCs), therefore, their catalytic performance is investigated in the following electrochemical measurements.

As seen in Fig. 5b, CV curves are obtained using a N_2 -saturated 0.5 M H_2SO_4 solution and recorded at a scan rate of 50 mV s^{-1} . The ECSAs are calculated by the integration of hydrogen adsorption peak area from the CV curves of Pt/C ($35.1 \text{ m}^2 \text{ g}_{\text{Pt}}^{-1}$), PtNiCo ($43.8 \text{ m}^2 \text{ g}_{\text{Pt}}^{-1}$) and PtCoNiMo ($48.7 \text{ m}^2 \text{ g}_{\text{Pt}}^{-1}$). The CO-stripping curves were also recorded at a scan rate of 50 mV s^{-1} , and the peak potential of PtCoNiMo NSs (0.485 V) exhibited a more negative potential, compared to PtCoNi NPs (0.504 V) and to commercial Pt/C (0.594 V) (Fig. 5c). The ratios between forward-scan and back-scan peaks are 0.98, 0.83 and 0.66 for PtCoNiMo NSs, PtCoNi NPs and Pt/C catalysts, respectively. The results further indicate that PtCoNiMo NSs catalyst exhibits enhanced anti-poisoning ability compared to Pt/C and PtCoNi NPs (Fig. 5d). Based on the oxidation peak intensity and Pt loadings for PtCoNiMo NSs (6.15 mA , $17.4 \text{ } \mu\text{g}_{\text{Pt}} \text{ cm}^{-2}$), PtCoNi NPs (6.44 mA , $19.4 \text{ } \mu\text{g}_{\text{Pt}} \text{ cm}^{-2}$) and Pt/C catalysts (2.59 mA , $30.6 \text{ } \mu\text{g}_{\text{Pt}} \text{ cm}^{-2}$), the PtCoNiMo NSs displayed for MOR a better mass activity ($1.82 \text{ A mg}_{\text{Pt}}^{-1}$), which was 4.2 times greater than that of commercial Pt/C ($0.43 \text{ A mg}_{\text{Pt}}^{-1}$) (Fig. 5f). In addition, the PtCoNiMo NSs have a more negative onset potential than other samples. The results show that PtCoNiMo NSs possess enhanced MOR catalytic activity and anti-poisoning ability than commercial Pt/C.

The ORR polarization curves were obtained under a scan rate of 10 mV s^{-1} in a 0.1 M HClO_4 solution. Compared with commercial Pt/C catalyst ($0.15 \text{ A mg}_{\text{Pt}}^{-1}$), the PtCoNiMo NSs ($0.45 \text{ A mg}_{\text{Pt}}^{-1}$) and PtCoNi

NPs ($0.22 \text{ A mg}_{\text{Pt}}^{-1}$) showed more positive onset potential and enhanced ORR catalytic activity at 0.9 V vs. RHE (Figs. 5e & 5f). The catalytic performance of the PtCoNiMo NSs catalyst should be attributed to the vertex-reinforced nanostructure, the Pt-rich surface and the introduction of Mo [8,14,45].

The durability of PtCoNiMo nano-skeletons (NSs) catalyst for MOR was measured through performing 1000 cycles of ADTs (Figs. 6a, S7 & S8). As seen in Figs. 6b & S9b, the mass activity of commercial Pt/C catalyst was reduced to 67.1% of the initial value after 1000 cycles, while the PtCoNiMo NSs catalyst was only reduced to 83.5% of the initial value. The results indicate that the PtCoNiMo NSs catalyst has an efficient mass activity, and the mass activity of PtCoNiMo NSs catalyst can still reach $1.51 \text{ A mg}_{\text{Pt}}^{-1}$, which was 5.2 times higher than that of commercial Pt/C catalyst (mass activity of $0.29 \text{ A mg}_{\text{Pt}}^{-1}$). In addition, the stability of PtCoNiMo NSs catalyst for ORR was investigated by using ADTs for 10,000 cycles (Figs. 6c & S10c) [46,47].

The TEM images and EDS atomic ratios of PtCoNiMo NSs before and after 10,000 cycles are shown in Figs. S11(c & d). The tip areas of PtCoNiMo NSs was slightly destroyed after the ADTs, and a large amount of Co was dissolved, resulting in the decrease of mass activity. As shown in Figs. 6d & S12, after 10,000 cycles the mass activity of PtCoNiMo NSs catalyst was reduced to 77.8% of the initial value, while the commercial Pt/C catalyst was reduced to 40.1% of the initial value. Remarkably, compared with the PtCoNi NPs, the PtCoNiMo NSs catalyst showed enhanced mass activity, stability and anti-poisoning ability for MOR and ORR due to the introduction of Mo and vertex-reinforced structure [45]. Based on the above discussion, the stability of the quaternary nano-skeletons catalyst is improved compared to commercial Pt/C catalysts and PtCoNi NPs. In our mind, the improvement in stability is mainly due to the following two points: 1) the Mo-modified multi-catalyst via alloying treatment is more stable than pure Pt catalysts and 2) the vertex-reinforced nano-skeletons structure is active than NPs due to better electron transfer and mass exchange. In addition, the quaternary catalyst still needs improvement, and the PtCoNiMo ND as superior bifunctional catalyst is promising in future work.

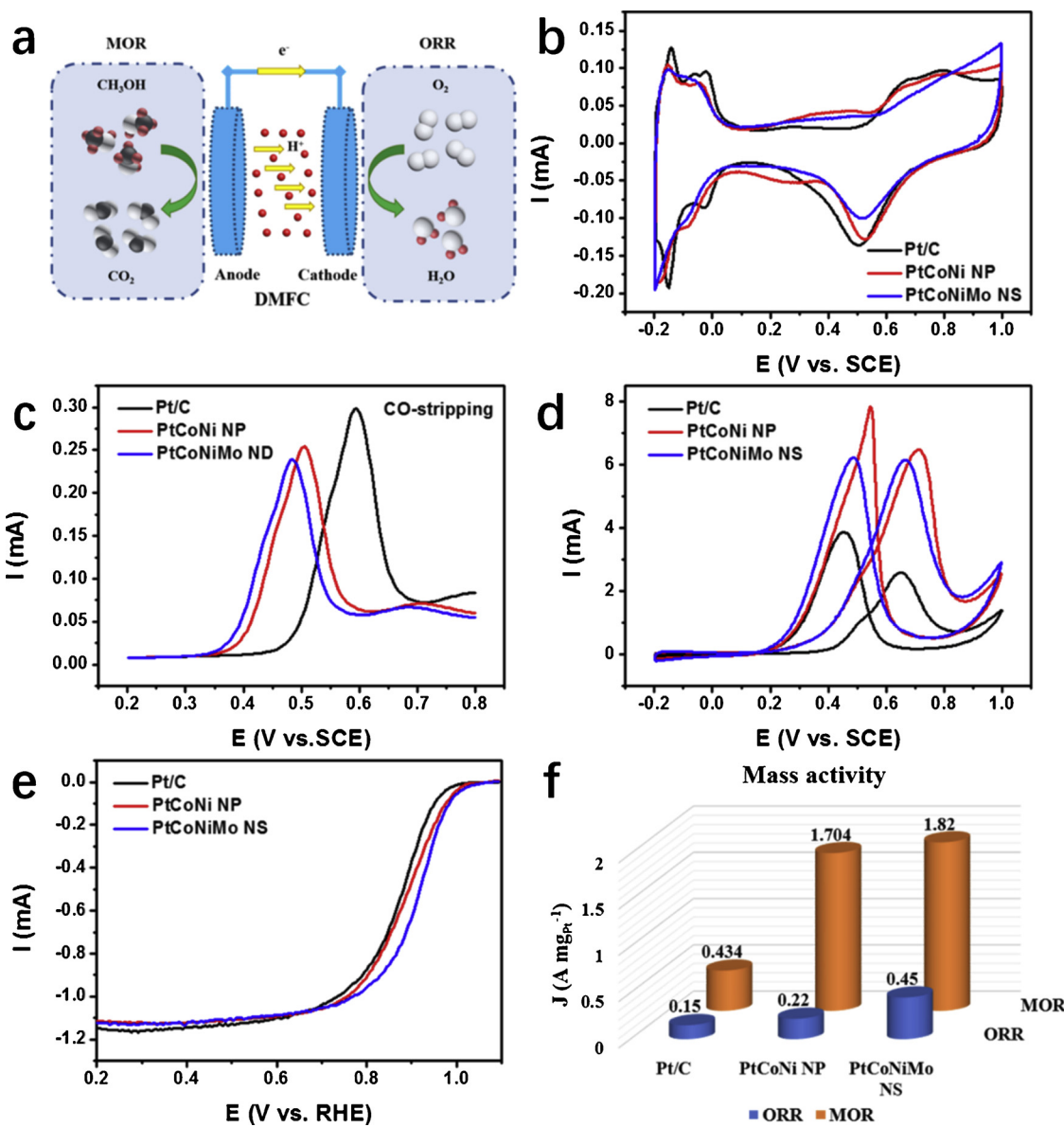


Fig. 5. (a) Schematic diagram of methanol oxidation reaction and oxygen reduction reaction processes. Electrochemical measurements of the PtCoNiMo NSs, PtCoNi NPs and Pt/C catalysts. (b) CV curves recorded in 0.5 M H₂SO₄ solution, (c) CO-stripping curves, (d) MOR curves recorded in 0.5 M H₂SO₄ + 1.0 M CH₃OH solution, (e) ORR polarization curves in 0.1 M HClO₄ solution, (f) mass activity towards MOR and ORR.

4. Conclusions

In summary, we have successfully prepared vertex-reinforced quaternary PtCoNiMo hexapod nano-skeletons (NSs) by Mo modification. It is noticeable that Mo(CO)₆ plays a key role in the synthesis process; only PtCoNi NPs can be obtained in absence of Mo(CO)₆. The quaternary PtCoNiMo hexapod NSs possess a series of tip areas with high-index facets, which can facilitate electron transfer, mass exchange and performance improvement. Meanwhile, the quaternary hexapod NSs are composed of core, first-layer feet and second-layer feet. The formation process of PtCoNiMo hexapod NSs is also analyzed with the progress of reaction time. Based on the advantages mentioned, compared with commercial Pt/C catalyst and PtCoNi NPs, quaternary PtCoNiMo hexapod NSs exhibit efficient mass activity, stability and anti-poisoning ability for MOR and ORR. More meaningfully, quaternary catalysts can offer more possibilities for the performance improvement of Pt-based catalysts.

Declaration of Competing Interest

The authors declare that they have no known competing financial interests or personal relationships that could have appeared to influence the work reported in this paper.

Acknowledgments

This work was supported by the Guangxi Science and Technology Project (AA17204083, AB16380030), National Basic Research Program of China (2015CB932304), the Natural Science Foundation of Guangdong Province (2015A030312007), the link project of the National Natural Science Foundation of China and Fujian Province (U1705252) and the Danish project of Initiative toward Non-precious Metal Polymer Fuel Cells (4106-000012B). Prof. Tsiakaras thankfully acknowledges co-financing by European Union & Greek national funds through the Operational Program Competitiveness, Entrepreneurship and Innovation, under the call RESEARCH – CREATE – INNOVATE (Project code: T1EDK-02442).

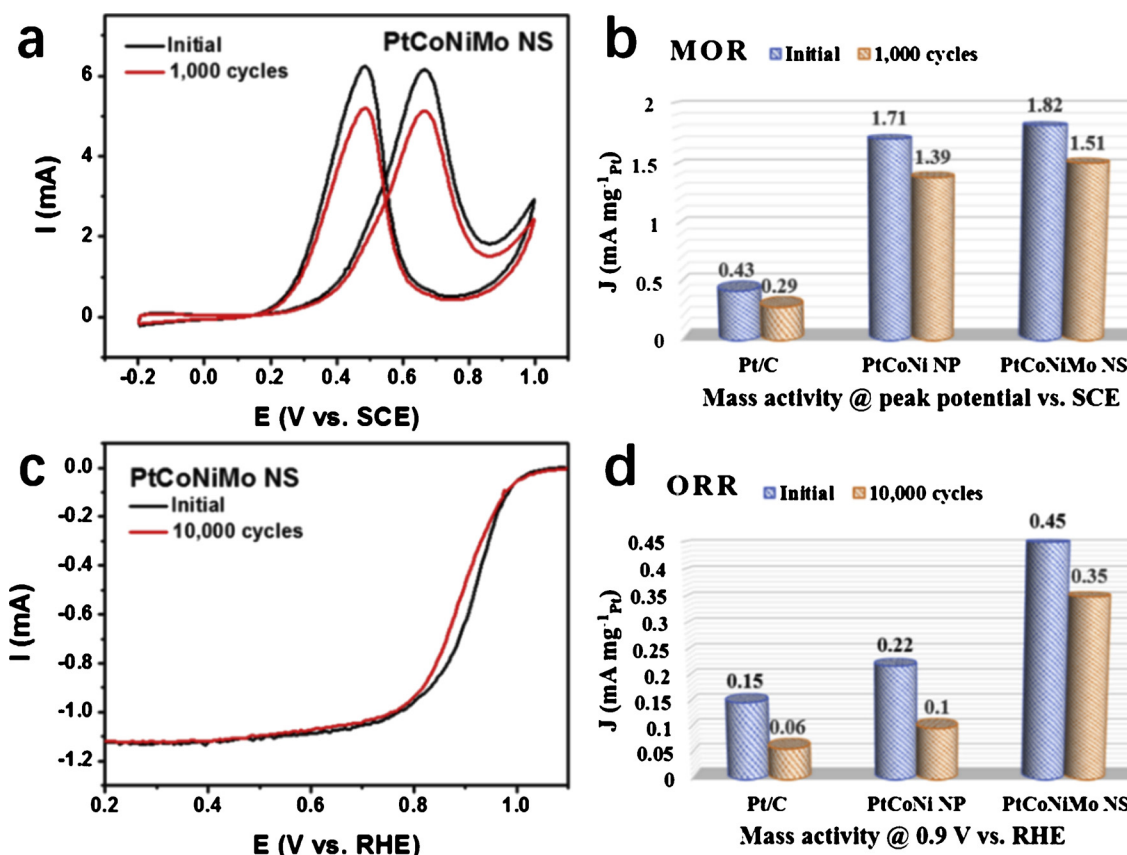


Fig. 6. (a) MOR curves, (b) mass activity at the peak potential vs. SCE before and after 1000 cycles. (c) ORR polarization curves, (d) mass activity at 0.9 V vs. RHE before and after 10,000 cycles.

Appendix A. Supplementary data

Supplementary material related to this article can be found, in the online version, at doi:<https://doi.org/10.1016/j.apcatb.2019.117974>.

References

- A. Kongkanand, M.F. Mathias, *J. Phy. Chem. Lett.* 7 (2016) 1127–1137.
- H.A. Gasteiger, S.S. Kocha, B. Sompalli, F.T. Wagner, *Appl. Catal. B: Environ.* 56 (2005) 9–35.
- M. Tang, S. Luo, K. Wang, H. Du, R. Sripathoorat, P.K. Shen, *Nano Res.* 11 (2018) 4786–4795.
- Y. Li, F. Quan, K. Chen, L. Chen, C. Chen, *Catal. Today* 278 (2016) 247–254.
- A. Brouzgou, S.Q. Song, P. Tsikararas, *Appl. Catal. B: Environ.* 127 (2012) 371–388.
- B.Y. Xia, H.B. Wu, X. Wang, X.W. Lou, J. Am. Chem. Soc. 134 (2012) 13934–13937.
- N. Becknell, Y. Son, D. Kim, D. Li, Y. Yu, Z. Niu, T. Lei, B.T. Sneed, K.L. More, N.M. Markovic, V.R. Stamenkovic, P. Yang, *J. Am. Chem. Soc.* 139 (2017) 11678–11681.
- L. Huang, Z. Jiang, W. Gong, P.K. Shen, *ACS Appl. Nano Mater.* 1 (2018) 5019–5026.
- G. Zhang, C. Huang, R. Qin, Z. Shao, D. An, W. Zhang, Y. Wang, *J. Mater. Chem. A Mater. Energy Sustain.* 3 (2015) 5204–5211.
- J.C. Calderón, G. García, L. Calvillo, J.L. Rodríguez, M.J. Lázaro, E. Pastor, *Appl. Catal. B: Environ.* 165 (2015) 676–686.
- C. Xu, Y. Du, C. Li, J. Yang, G. Yang, *Appl. Catal. B: Environ.* 164 (2015) 334–343.
- L. Huang, Z. Jiang, W. Gong, Z. Wang, P.K. Shen, *J. Power Sources* 406 (2018) 42–49.
- T. Kwon, M. Jun, H.Y. Kim, A. Oh, J. Park, H. Baik, S.H. Joo, K. Lee, *Adv. Funct. Mater.* 28 (2018) 1706440.
- R. Sripathoorat, K. Wang, S. Luo, M. Tang, H. Du, X. Du, P.K. Shen, *J. Mater. Chem. A Mater. Energy Sustain.* 4 (2016) 18015–18021.
- S.Y. Ma, H.H. Li, B.C. Hu, X. Cheng, Q.Q. Fu, S.H. Yu, *J. Am. Chem. Soc.* 139 (2017) 5890–5895.
- Sean T. Hunt, Maria Milina, Ana C. Alba-Rubio, Christopher H. Hendon, James A. Dumesic, Y. Román-Leshkov, *Science* 352 (2016) 974–978.
- S. Guo, S. Zhang, D. Su, S. Sun, *J. Am. Chem. Soc.* 135 (2013) 13879–13884.
- C. Wang, C. Lin, L. Zhang, Z. Quan, K. Sun, B. Zhao, F. Wang, N. Porter, Y. Wang, J. Fang, *Chemistry* 20 (2014) 1753–1759.
- H. Zhu, S. Zhang, S. Guo, D. Su, S. Sun, *J. Am. Chem. Soc.* 135 (2013) 7130–7133.
- S. Guo, D. Li, H. Zhu, S. Zhang, N.M. Markovic, V.R. Stamenkovic, S. Sun, *Angew. Chem. Int. Ed.* 52 (2013) 3465–3468.
- C. Wang, Y. Hou, J. Kim, S. Sun, *Angew. Chem.* 119 (2007) 6449–6451.
- S. Guo, S. Zhang, X. Sun, S. Sun, *J. Am. Chem. Soc.* 133 (2011) 15354–15357.
- Q. Xiao, M. Cai, M.P. Balogh, M.M. Tessema, Y. Lu, *Nano Res.* 5 (2012) 145–151.
- S.I. Lim, I. Ojea-Jiménez, M. Varon, E. Casals, J. Arbiol, V. Puntes, *Nano Lett.* 10 (2010) 964–973.
- S. Mourdikoudis, I.M. Liz-Marzán, *Chem. Mater.* 25 (2013) 1465–1476.
- L. Huang, X. Zhang, Y. Han, Q. Wang, Y. Fang, S. Dong, *Chem. Mater.* 29 (2017) 4557–4562.
- C. Wang, L. Zhang, H. Yang, J. Pan, J. Liu, C. Dotse, Y. Luan, R. Gao, C. Lin, J. Zhang, J.P. Kilcrease, X. Wen, S. Zou, J. Fang, *Nano Lett.* 17 (2017) 2204–2210.
- B.Y. Xia, H.B. Wu, X. Wang, X.W. Lou, *Angew. Chem. Int. Ed.* 52 (2013) 12337–12340.
- Y. Qi, T. Bian, S.I. Choi, Y. Jiang, C. Jin, M. Fu, H. Zhang, D. Yang, *Chem. Commun.* 50 (2014) 560–562.
- K. Wang, R. Sripathoorat, S. Luo, M. Tang, H. Du, P.K. Shen, *J. Mater. Chem. A Mater. Energy Sustain.* 4 (2016) 13425–13430.
- K. Wang, H. Du, R. Sripathoorat, P.K. Shen, *Adv. Mater.* (2018) 1804074.
- L.-M. Lyu, Y.-C. Kao, D.A. Cullen, B.T. Sneed, Y.-C. Chuang, C.-H. Kuo, *Chem. Mater.* 29 (2017) 5681–5692.
- S. Luo, M. Tang, P.K. Shen, S. Ye, *Adv. Mater.* 29 (2017) 1601687.
- V. Stamenkovic, B.S. Mun, K.J. Mayrhofer, P.N. Ross, N.M. Markovic, J. Rossmeisl, J. Greeley, J.K. Norskov, *Angew. Chem., Int. Ed.* 45 (2006) 2897–2901.
- J. Greeley, I.E. Stephens, A.S. Bondarenko, T.P. Johansson, H.A. Hansen, T.F. Jaramillo, J. Rossmeisl, I. Chorkendorff, J.K. Norskov, *Nat. Chem.* 1 (2009) 552–556.
- D. Wang, H.L. Xin, R. Hovden, H. Wang, Y. Yu, D.A. Muller, F.J. DiSalvo, H.D. Abruna, *Nat. Mater.* 12 (2013) 81–87.
- L. Gan, C. Cui, M. Heggen, F. Dionigi, S. Rudi, P. Strasser, *Science* 346 (2014) 1502–1506.
- A. Oh, H. Baik, D.S. Choi, J.Y. Cheon, B. Kim, H. Kim, S.J. Kwon, S.H. Joo, Y. Jung, K. Lee, *ACS Nano* 9 (2015) 2856–2867.
- F. Tao, S. Dag, L.-W. Wang, Z. Liu, D.R. Butcher, M. Salmeron, G.A. Somorjai, *Nano Lett.* 9 (2009) 2167–2171.
- D.R. Butcher, M.E. Grass, Z. Zeng, F. Aksoy, H. Bluhm, W.X. Li, B.S. Mun, G.A. Somorjai, Z. Liu, *J. Am. Chem. Soc.* 133 (2011) 20319–20325.
- C. Wang, H. Daimon, T. Onodera, T. Koda, S. Sun, *Angew. Chem., Int. Ed.* 47 (2008) 3588–3591.
- B. Wu, N. Zheng, G. Fu, *Chem. Commun.* 47 (2011) 1039–1041.
- J. Zhang, J. Fang, *J. Am. Chem. Soc.* 131 (2009) 18543–18547.
- C. Wang, H. Daimon, Y. Lee, J. Kim, S. Sun, *J. Am. Chem. Soc.* 129 (2007) 6974–6975.
- X. Huang, Z. Zhao, L. Cao, Y. Chen, E. Zhu, Z. Lin, M. Li, A. Yan, A. Zettl, Y.M. Wang, X. Duan, T. Mueller, Y. Huang, *Science* 348 (2015) 1230–1234.
- X. Tuav, S. Rudi, V. Petkov, A. Hoell, P. Strasser, *ACS Nano* 7 (2013) 5666–5674.
- W.S. Jung, B.N. Popov, *ACS Appl. Mater. Interfaces* 9 (2017) 23679–23686.